UNIVERSITY OF BATH

University of Bath

Research

CrossMark
click for updates

Author for correspondence:

N.Y.Bailey

e-mail: N.Y.Bailey@bath.ac.uk

Nonlinear flexure coupling elements for precision control of multibody systems

N. Y. Bailey[1], C. Lusty[1] and P. S. Keogh[1]

[1]Department of Mechanical Engineering, University of Bath, Bath, BA2 7AY.

Conventional multibody systems used in robotics and automated machinery contain bearing components that exhibit complex and uncertain tribological characteristics. These limit fundamentally the precision of the automated motion and also cause wear. Replacing traditional bearing joints with flexure couplings eliminates these tribological effects, together with wear, reducing necessary system maintenance and offering a potential for increased motion precision. A flexure-coupled multibody system is considered and a novel general solution technique is presented. Derivation of a large deflection flexure coupling model is provided and subsequently validated using an experimental facility. A focused study of a unique double flexure coupling-rigid body system is given; the formulated nonlinear mathematical model can be utilised for feedforward control. Equivalent control is also applied to a corresponding system with traditional bearing joints. The feasibility of replacing bearing joints by flexure couplings is demonstrated in terms of accurate large displacement control and reduction of high frequency disturbances.

1. Introduction

Conventional multibody mechanisms, typically comprising a number of rigid bodies connected through translating and/or rotary joints, are used widely in robotics and automated machinery. These enable industrial processes that depend on fast and precisely controlled motion, such as the assembly and inspection of manufactured products.

Currently, manufacturing techniques for high added-value components of complex products, such as in the automotive and aerospace industries, require jigs to ensure precision and repeatability of the manufacturing process, allowing for interchangeability of parts. However, jigs are expensive to produce and are inflexible; one small adjustment in the manufacture of a component may require an extensive modification to a jig.

One way to improve the manufacturing process, making it more flexible and cost effective whilst maintaining the accuracy and repeatability, is to introduce robotics and sensors. This has been the recent trend in manufacturing, with the overall aim of achieving high-added value products and systems of high precision.

The efficiency and precision of robotic systems is limited by complex and uncertain tribological effects within traditional bearing joints, including backlash, stiction, friction, torque ripple and compliance. These joints generally experience wear, causing degradation of performance over a period of operation. Combining multiple joints in a single mechanism compounds the individual effects from each joint, resulting in larger uncertain tribological effects overall. In turn, these effects limit device capability to accurately follow desired displacement, velocity or acceleration profiles. It is difficult to compensate for these uncertain and nonlinear effects with active control. However, the source of these effects may be eliminated through new designs of multibody mechanisms containing compact deformable structures, also known as flexure couplings. They facilitate movement between rigid bodies through elastic deformation, which is not subject to wear nor requires lubrication. However, flexure couplings introduce additional degrees of freedom in which a mechanism can undergo dynamic motion, resulting in systems with complex mechanical behaviour. Nevertheless, with accurately predicted flexure coupling behaviour, suitable actuation and control methodology, precise and repeatable motion of a mechanism should be achievable, without oscillations or instabilities.

Flexure couplings are common in micro- and nano-positioning mechanisms, due to their capacity for high positioning accuracy together with robustness against parasitic motion errors and external disturbances [1,2]. Other advantages include preventing low frequency excitation of components due to their increased stiffness compared to traditional joints [3], resulting in precise and repeatable motion. On a larger scale, bearing joints have already been replaced with flexure couplings in some robotic mechanisms. For example, there has been significant research into the design of low-complexity, compliant, adaptive robot hands for grasping and dexterous manipulation. This includes stable, minimal effort grasps of robotic hands incorporating parasitic object motion compensation post-contact [4], medium-complexity robot hand to allow for delicate fingertip grasps and medium-dexterity manipulation tasks to be performed [5]. Adaptive robot grippers with haptic object properties and an ability to identify objects during a single functional grasp have also been examined [6]. Solid-state hinges have been investigated to replicate the function of conventional bearings for both rotational and translational motions [7]. These have increased off-axis stiffness and minimal axis drift, while achieving a larger range of motion than conventional flexure joints. The complete range of motion is determined by the material and geometry of the joint.

For a mechanism containing flexure couplings to achieve a prescribed trajectory under active control, the higher order nonlinear elastodynamics of the flexure coupling must be accounted for in the controller design. Thus, a model-based controller is ideal. Simplified models have been used to examine systems containing a combination of flexure joints and rigid bodies, forming pseudo-kinematic chains, which are typically based on pseudo-rigid-body models; the flexure is represented as a serial-chain of rigid bodies connected with passive elastic joints. A majority of this work focuses on applications with very small displacements [8]. However, an elastic rod fixed at both ends, modelled using this methodology and represented by a set of nonlinear equations derived by discretising differential equations and appropriate boundary conditions gave good correspondence with experimental results [9]; the author did state more work is needed on error analysis for more accurate shape estimation. Guo and Lee [10] presented an equivalent pin model, which accounted for the moving centre of rotation in the coupling and the varying radius of a compliant joint. In order to have a realistic prediction of the flexure couplings, they may need to be limited in length [11].

More accurate predictions of the flexure behaviour, especially when the flexure undergoes large deformation, are needed for use in model-based controller design. Previously, large deflections of a flexible link have been studied extensively when modelled as a nonlinear cantilever beam experiencing an external force (tip concentrated and/or distributed loads) in the steady case, using the arc length coordinate system. Many different methods have been implemented, including the analytical Homotopy Analysis Method [12,13] as well as numerical techniques such as, the finite-element method [14]; a smooth curvature model [15]; an elliptic-function solution combined with the shooting method [16,17]; a fourth-order Runge-Kutta method [18,19]; a beam-constraint model [20] and a finite difference method [21]. Although analysis

of a cantilever beam undergoing large deflections is extensive, models combining these with rigid bodies, to form pseudo-kinematic chains are very limited. Lobontiu [22] examined the dynamics of a four-link pendulum, which was excited by gravity alone and consisted of two rigid segments and two flexure couplings, although these were assumed to have small deformation. The dynamics of an elastica catapult using a quasi-static response for low acceleration was considered by Armanini et al. [23] where finite element software analysis, Abaqus, was used for the passive catapult response.

Control of a compact deformable structure undergoing large deflections has been analysed by Gravagne et al. [24] where a vibration-damping setpoint controller was applied to a planar continuum backbone section to attenuate vibrations. Meanwhile, Moallem et al. [25] examined a flexible link manipulator with a payload, using piezoelectric transducers as both an actuator and sensor elements, and implemented control using a linear-quadratic regulator. A control scheme based on partial feedback linearisation to regulate the forces exerted by a smart memory alloy actuator pair attached to a flexible beam to control the tip of the beam was examined by Moallem and Lu [26]. Flexure couplings are not currently used in mechanisms which subject to motion control due to their complex behaviour and current lack of understanding of their dynamics.

This paper considers new approaches to mechanism and controller design for systems incorporating large deflection flexure couplings. The nonlinear elastodynamics introduced by flexure couplings need to be accounted for in the controller designed to regulate the actuation forces and thereby achieve accurate motion tracking. The mathematical formulation of a generic flexure-coupled multibody system is given in Section 2. Section 3 contains the derivation of a mathematical model for large deformation of a beam like flexure coupling which is subsequently validated using an experimental test facility. A focused study of a multi-rigid body system incorporating these flexure couplings is given in Section 4. A dynamic mathematical model is formulated and comparison is drawn between the theoretical predictions and experimental results. In Section 5, control methodology is developed using open-loop feedforward control derived from the mathematical model. The accuracy of controlling the trajectory of a multi-rigid body system containing flexure couplings is examined to demonstrate their potential in motion control systems.

2. Flexure coupled multibody system

An extended multibody system incorporating flexure couplings, such as in the generic schematic of Figure 1, is examined. Each dynamic subsystem n, has a control force, $\mathbf{u}_n$, applied to it and may be subject to external disturbance, denoted by $\mathbf{d}_n$. A dynamic subsystem may have a single or multiple flexure couplings to other subsystems. The coordinates of the position that the flexure couples to a system is indicated by $\mathbf{x}_{ni}$, where i is the index of the subsystem attached to the other end of the flexure. The dynamic subsystem is described by the state space form

$$\dot{\mathbf{z}}_n = \mathbf{A}_n\mathbf{z}_n + \mathbf{B}_n\mathbf{u}_n + \tilde{\mathbf{B}}_n\mathbf{d}_n - \sum_{\substack{m=1 \\ m\neq n}}^{N} \hat{\mathbf{B}}_{nm}\mathbf{f}_{nm},$$

$$\mathbf{x}_{ni} = \mathbf{C}_{ni}\mathbf{z}_n + \mathbf{D}_{ni}\mathbf{u}_n + \tilde{\mathbf{D}}_{ni}\mathbf{d}_n - \sum_{\substack{m=1 \\ m\neq n}}^{N} \hat{\mathbf{D}}_{nmi}\mathbf{f}_{nm}, \quad \forall i \neq n. \tag{2.1}$$

In the set of equations (2.1), $\mathbf{z}_n$ denotes the position and velocity states of the subsystem n, and $\mathbf{f}_{nm}$ the internal force from the flexure attached to subsystem m experienced by the subsystem n. Matrix $\mathbf{A}_n$ denotes the subsystem matrix and $\mathbf{B}_n$, $\tilde{\mathbf{B}}_n$ and $\hat{\mathbf{B}}_{nm}$ are the input matrices for the control, disturbance and internal forces, respectively. $\mathbf{C}_i$ is the output matrix and $\mathbf{D}_{ni}$, $\tilde{\mathbf{D}}_{ni}$ and $\hat{\mathbf{D}}_{nmi}$ are feedforward matrices for the control, disturbance and internal forces, respectively.

The state vector solution is given by

$$\mathbf{z}_n(t) = \mathbf{z}_n(0)e^{\mathbf{A}_n t} + \int_0^t e^{\mathbf{A}_n(t-\tau)}\left(\mathbf{B}_n\mathbf{u}_n(\tau) + \tilde{\mathbf{B}}_n\mathbf{d}_n(\tau) - \sum_{\substack{m=1 \\ m\neq n}}^{N} \hat{\mathbf{B}}_{nm}\mathbf{f}_{nm}(\tau)\right)d\tau, \tag{2.2}$$
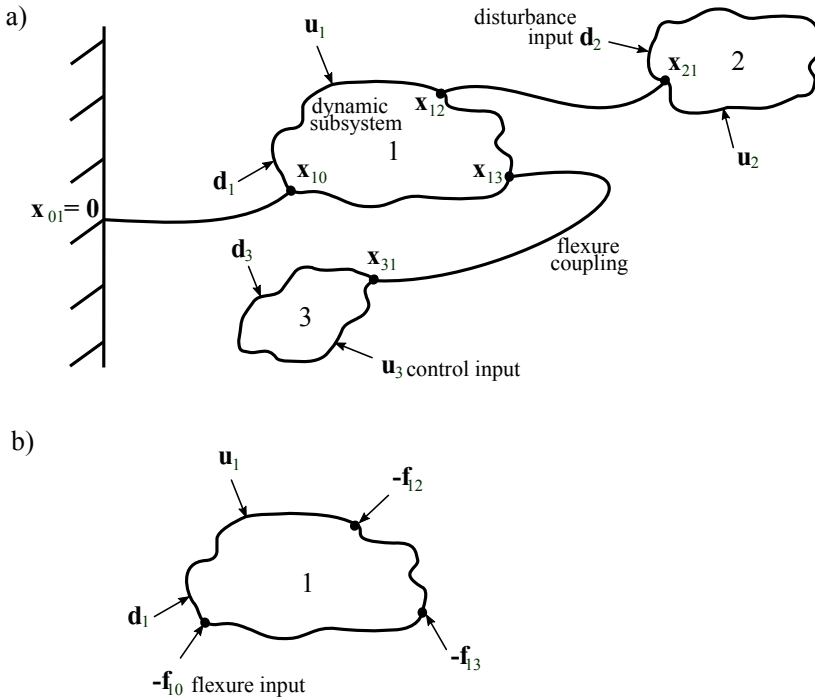
Figure 1. Schematics of a) flexure-coupled system under control with flexure and disturbance forces (inputs) and b) free body diagram of a subsystem.
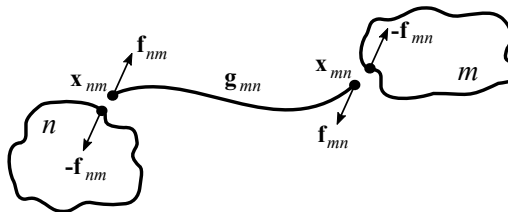

Figure 2. Generic motion of a flexure coupling deformation.

and the system output response is computed by substituting the expression for $\mathbf{z}_n$ into the equation for $\mathbf{x}_{ni}$ in (2.1).

The relationship between the dynamic subsystems is defined by the flexure coupling, as shown in the schematic of Figure 2, which is given by

$$\mathbf{x}_{10} = \mathbf{g}_{10}(\mathbf{f}_{10}), \quad \mathbf{x}_{mn} - \mathbf{x}_{nm} = \mathbf{g}_{mn}(\mathbf{f}_{mn}), \quad \forall\, n \neq m. \tag{2.3}$$

where $\mathbf{g}_{mn}$ is the function defining the flexure deformation and $\mathbf{x}_{01} = \mathbf{0}$ (see Figure 1). Therefore the dynamics of the flexure-coupled multibody system are defined by the set of linear equations for the dynamic subsystems (2.1) and nonlinear equations for the flexure couplings (2.3).

3. Large deflections of a planar flexure coupling

A model of a planar flexure coupling undergoing large deflections is derived from the nonlinear Euler-Bernoulli beam theory [27]. In this case the deformation is assumed to be bending primarily with shear and axial deformations negligible due to the flexure coupling having significantly larger width and length
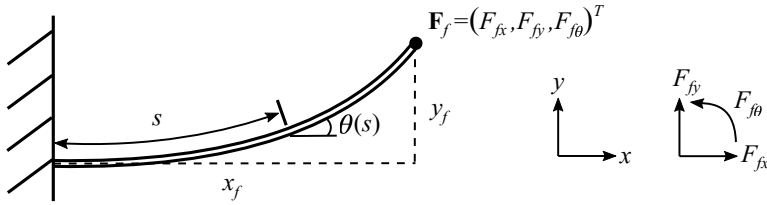
Figure 3. Schematic diagram for a flexure coupling in planar motion with force $\mathbf{F}_f = (F_{fx}, F_{fy}, F_{f\theta})^T$ imposed at the end.

than thickness. The flexure material is assumed to be linear-elastic isotropic and is treated as prismatic with constant cross-sectional area A and second moment of area I. The axial stiffness EA of the beam is very high when compared to bending stiffness EI, where E is the Young's modulus, and thus the flexure is considered to experience negligible axial strains.

A set of forces and a moment $\mathbf{F}_f = (F_{fx}, F_{fy}, F_{f\theta})^T$ is imposed at the tip of the flexure at the centreline, as shown in Figure 3; regardless of the flexure deflection, F_{fx} and F_{fy} are applied in the x and y directions, respectively. The arc length coordinate $s := [0, l_f]$ is introduced in two-dimensional Euclidean space along the flexure centreline to define Cartesian coordinates that give rise to geometric nonlinearities [28]. The Cartesian coordinates at a given length s along the flexure, with angle of deflection $\theta(s)$, are given by

$$x(s) = \int_0^s \cos\theta(u)du, \qquad y(s) = \int_0^s \sin\theta(u)du. \tag{3.1}$$

At the flexure tip, i.e. when $s = l_f$, the coordinates are denoted by $\mathbf{x}_f = (x_f, y_f, \theta_f)^T$.

A model for the flexure coupling is formulated using the classical Euler-Bernoulli hypothesis for large deformations, where the bending moment at any point of the beam is proportional to the corresponding curvature. The resulting equation is

$$EI\frac{d\theta}{ds} = M(s) = -F_{fx}(y_f - y(s)) + F_{fy}(x_f - x(s)) + F_{f\theta}, \tag{3.2}$$

where $M(s)$ denotes the moment at $(x(s), y(s))$.

The governing equation for the flexure is found by differentiating equation (3.2) with respect to the arc length s, resulting in the second order nonlinear differential equation for the angle,

$$\frac{d^2\theta}{ds^2} = \frac{1}{EI}\frac{dM}{ds} = \frac{1}{EI}\left(F_{fx}\sin\theta - F_{fy}\cos\theta\right), \tag{3.3}$$

using the relations $dx/ds = \cos\theta$ and $dy/ds = \sin\theta$ from (3.1). Boundary conditions are $\theta(0) = 0$ and $d\theta(l_f)/ds = F_{f\theta}/EI$ as the flexure is assumed fixed at $s = 0$ with zero angle and curvature at the free end is as given in equation (3.2). Therefore, the flexure can be characterised by θ, alone.

Rewriting the flexure governing equation (3.3) as a system of first order ordinary differential equations and combining with the expressions for the Cartesian coordinates (3.1), results in a system of first order differential equations

$$\frac{dz_1}{ds} = z_2, \quad \frac{dz_2}{ds} = \frac{1}{EI}\left(F_{fx}\sin z_1 - F_{fy}\cos z_1\right), \quad \frac{dx}{ds} = \cos z_1, \quad \frac{dy}{ds} = \sin z_1, \tag{3.4}$$

where $\theta = z_1$ and $d\theta/ds = z_2$. Corresponding boundary conditions are given by

$$z_1(0) = 0, \quad z_2(l_f) = \frac{F_{f\theta}}{EI}, \quad x(0) = 0, \quad y(0) = 0. \tag{3.5}$$

For a sufficiently accurate initial estimate, the system of equations (3.4) and (3.5), can be solved using a finite difference method implementing a three-stage Lobatto IIIa formula.

Possible positions of a flexure coupling experiencing actuation from the set of forces and moment $\mathbf{F}_f$, are given in Figure 4 for different combinations of F_{fy} and $F_{f\theta}$ with F_{fx} fixed at 0 N; if $\mathbf{F}_f = \mathbf{0}$, the flexure is aligned along the x axis. A flexure coupling of length $l_f = 30$ mm and thickness $h_f = 0.4$ mm is examined with elastic modulus $E = 193 \times 10^9$ N/m^2 and second moment of area $I = 1.6 \times 10^{-13}$ m^4. Figure 4 shows
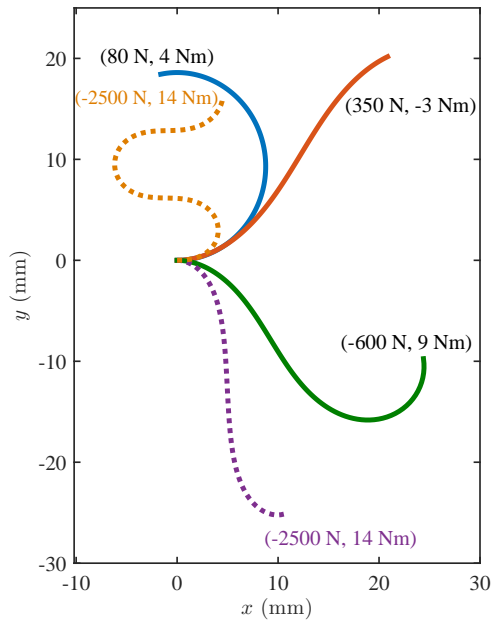
Figure 4. Possible flexure coupling deflections for force/moment combination $(F_{fy}$ N, $F_{f\theta}$ Nm); $F_{fx} = 0$ N. Note that the two dotted lines have identical external force combinations but different deflected shapes are predicted with different initial estimates.

a variety of possible flexure deflections and highlights that a flexure coupling may adapt different shapes under the same applied force $\mathbf{F}_f$.

Similarly, for a given end position of the flexure there are multiple forces $\mathbf{F}_f$ which can achieve this position. Therefore, for independent actuation of the components of $\mathbf{F}_f$, a many-to-many relationship between the force and tip position dictates that the flexure coupling cannot be solved in an inverse manner, i.e. for a given end position of the flexure a unique force vector required to achieve this position does not exist.

(a) Validation of flexure coupling model

The mathematical model for a flexure coupling is validated using the experimental set up shown in Figure 5a). The flexure coupling is made from fully hardened grade 301 stainless steel with a length and width of 30 mm and thickness 0.4 mm; it is clamped in place at either end between two blocks of aluminium with dowling rods to prevent the flexure coupling moving.

A lead screw actuator provides the force to deflect the flexure coupling via a linkage mechanism, which is modelled as a series of rigid elements connected with perfect hinges as shown in Figure 5b). The extension of the actuator rod is l_0, l_p is the length of the flexure clamp which is parallel to the link of length l_2 and separated by a perpendicular length of l_v. Both the flexure clamp and link l_2 have the same angle as the end of the flexure coupling, θ_f. The length of linkage between the two joints is l_1 at angle ϕ; the joints in the experimental set up are deep groove ball bearings and a linear bearing is used on the actuator rod to minimise the effects of side loading. The force $-\mathbf{F}_f$ is applied by the flexure.

In Figure 5b), the effect of the actuator force F_A is to impose an equivalent force $\mathbf{F} = (F_N, F_M, M_C)^T$ at the point shown. If F_A and $\mathbf{F}$ are in equilibrium then

$$F_N = F_A, \qquad F_M = F_A \tan\phi, \qquad M_C = \frac{F_A(l_2 \sin(\theta_f - \phi) + l_v \cos(\theta_f - \phi))}{\cos\phi}. \qquad (3.6)$$
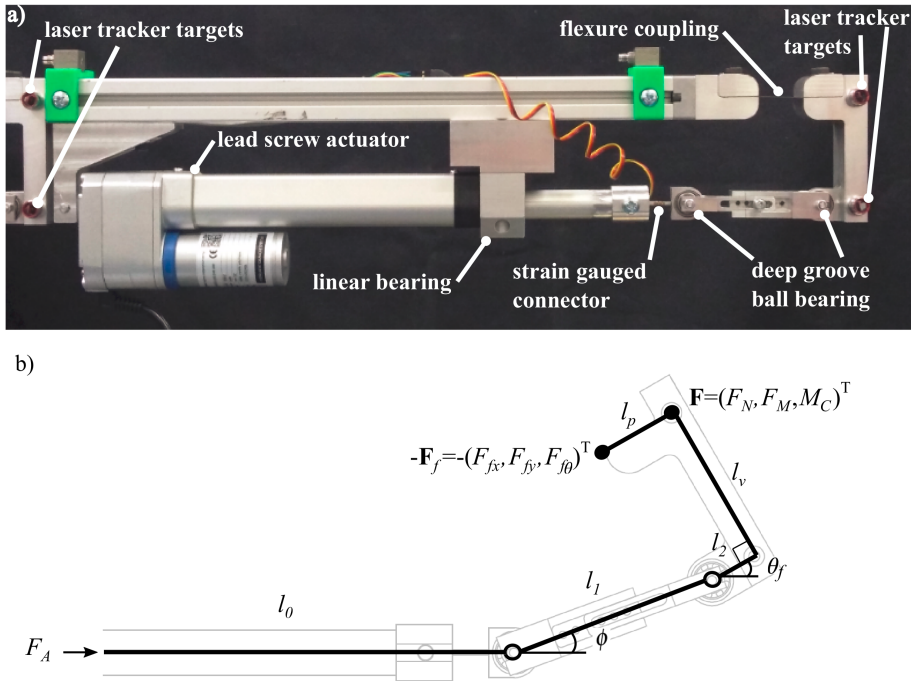
Figure 5. a) Experimental facility to validate flexure model and b) linkage mechanism for the first joint. The force pairs $(F_A, \mathbf{F})$ and $(\mathbf{F}, -\mathbf{F}_f)$ are in equilibrium.

The equilibrium of $\mathbf{F}$ and $-\mathbf{F}_f$ yields

$$F_{fx} = F_N, \qquad F_{fy} = F_M, \qquad F_{f\theta} = M_C + F_M l_p \cos\theta_f - F_N l_p \sin\theta_f. \qquad (3.7)$$

The angle ϕ and extension of actuator rod l_0 are defined by the system geometry

$$l_0 + \kappa + l_1 \cos\phi = x_f + (l_p - l_2)\cos\theta_f + l_v \sin\theta_f,$$

$$l_1 \sin\phi + l_v \cos\theta_f = y_f + (l_p - l_2)\sin\theta_f + l_v, \qquad (3.8)$$

where κ is the offset of the start of l_0 to the fixed end of the flexure.

The linear actuator input is the actuator rod extension l_0 whereas the model input is the force from the actuator F_A. Therefore, experimental results were obtained by displacing the actuator rod by increments of 5 mm and recording the force and position measurements. The force measurements were achieved through a calibrated strain gauged connector in the actuation mechanism as shown in Figure 5a). The position of the system was detected using a 3D laser tracker; four laser tracker targets were positioned on the system as shown in Figure 5a). Figure 6 shows photographs of the system in different states of deflection with actuator rod extensions: a) 111.6 mm, which gives $\theta_f = 0$; b) maximum extension 166.6 mm; and c) minimum extension 56.6 mm. Note that the linear bearing prevented any further retraction of the linear actuation rod. Corresponding theoretical predictions of the deformed flexure coupling were found by inputting the measured forces into the model and computing the flexure tip angle and extension of the actuator rod.

The average of three experimental repeats, together with the model predications for actuator rod extension l_0 against angle θ_f and actuator force F_A against actuator rod extension l_0, are given in Figure 7 for a flexure coupling, a loosely fitted plain bushing hinge and a tightly press-fitted rolling element bearing hinge. For the case of the flexure coupling the relationship between the actuator rod extension against flexure tip angle has a good correlation between the experimental results and model predictions over the range of rod extensions examined. The case of actuator force against actuator rod extension has good correlation between the experimental results and model predictions when the actuator rod extension is around the
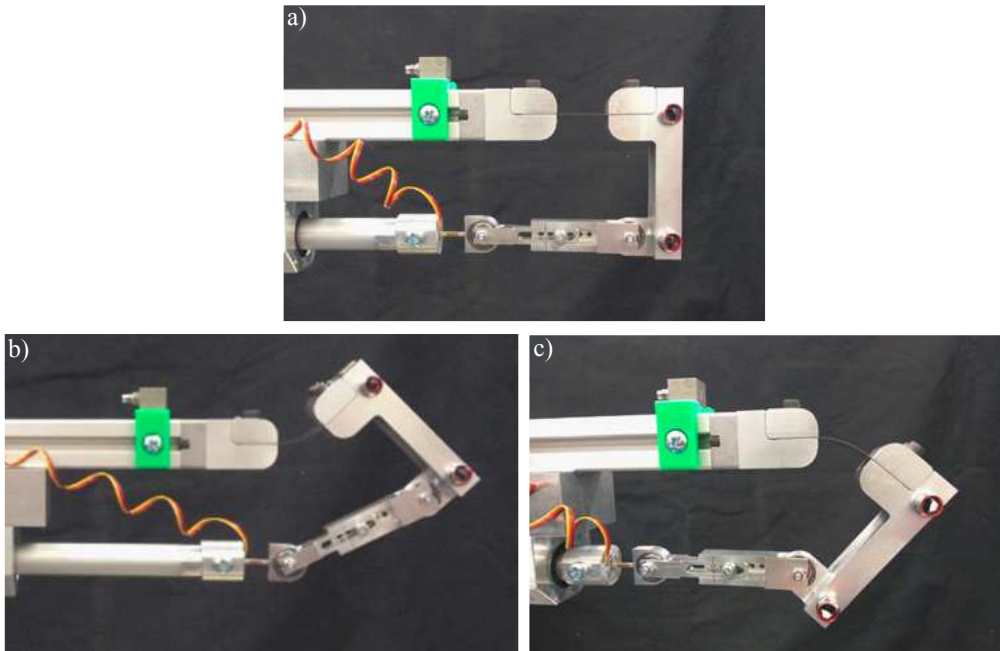
Figure 6. Flexure coupling in different states of deflection with actuator rod extensions: a) 111.6 mm giving $\theta_f = 0$; b) maximum extension 166.6 mm; and c) minimum extension 56.6 mm.

middle extension (111.6 mm). However, increasing or decreasing the actuator rod extension such that large angles are achieved, gives rise to a discrepancy between the experimental results and model predictions; this is due to the lateral load experienced by the actuation linkage mechanism (not measured). The results show there is a one-to-one relationship between the input force F_A, the actuator rod extension l_0 and the angle at the end of the flexure coupling, θ_f.

The force, F_A, is implicit for control purposes as the input is the actuator rod extension and the output is the deflection of the flexure coupling. Therefore, the discrepancy between the experimental results and the model predictions in the actuator force and extension relationship, shown in Figure 7b), should not affect the motion control of the system.

Corresponding results for conventional revolute bearing hinges show that there is good agreement between the angle θ_f and the actuator rod extension l_0. This is expected as it is dependent on the geometry of the actuation linkage in the static case. Examining the input force F_A against actuator extension l_0 gives poor correlations between the prediction and experimental results due to the lateral loading which the hinged system applies to the strain-gauged connector. The experimental system was designed for validation of the flexure coupling from which lateral loading will be lower. It is noted that the range of F_A for the hinged systems are lower than for the flexure coupling because the actuator force must overcome the flexure stiffness.

4. Large deflections of flexure coupled rigid bodies in series

To examine the feasibility of implementing flexure couplings into an automated system, an experimental facility comprising two rigid body links was constructed. A corresponding mathematical model was formulated, to enable design of an effective controller to regulate the motion of the system. The experimental system is presented first, followed by a detailed derivation of a model for a single flexure coupling-rigid body system and the governing equations of a double flexure coupling-rigid body system.
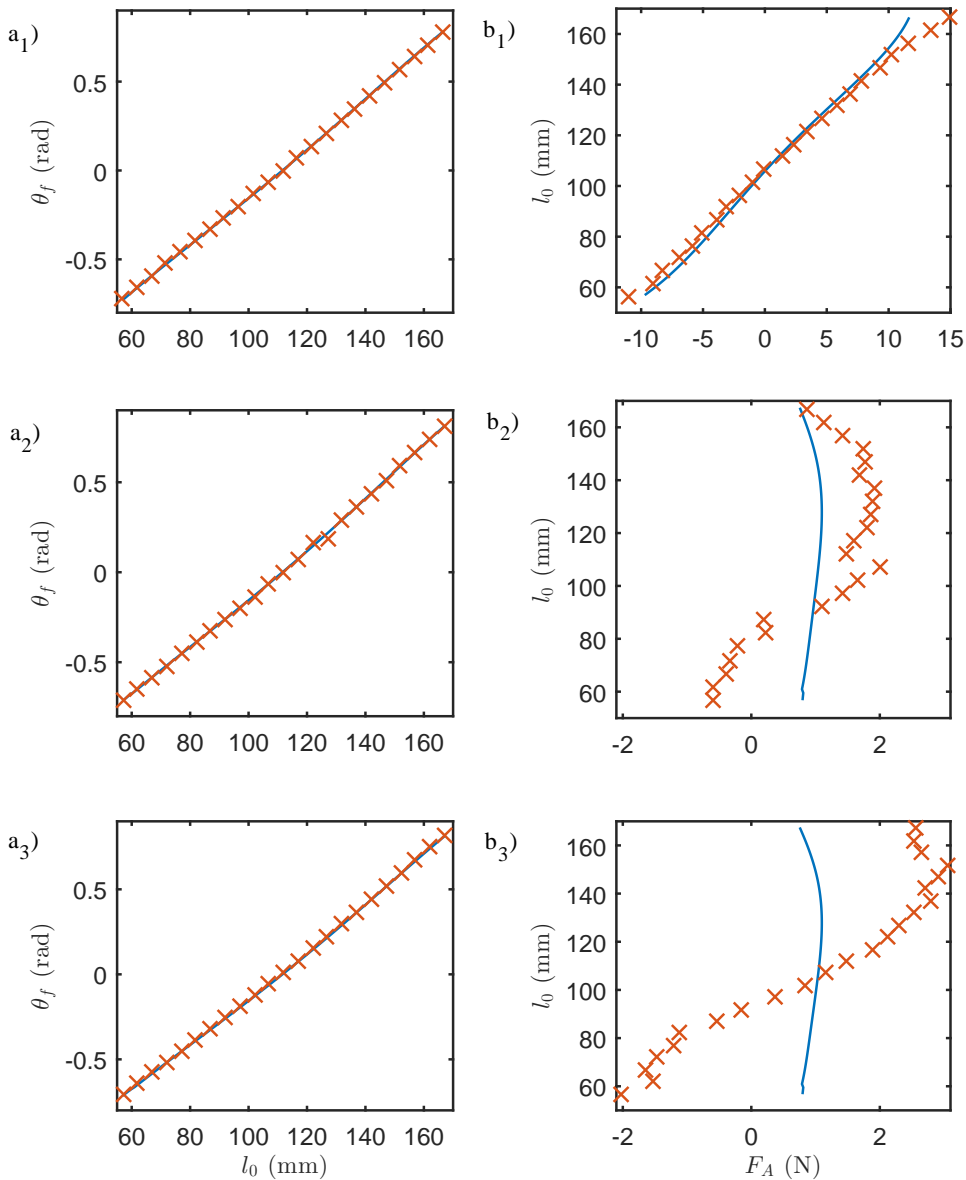
Figure 7. Experimental results (X) and model predications (—) for a) angle θ_f against actuator extension l_0 and b) actuator extension l_0 against actuator force F_A for 1) a flexure coupling, 2) a loosely fitted plain bushing hinge and 3) a tightly press-fitted rolling element bearing hinge. Parameter values are in the right hand side of Table 1 and the hinge length is the same as the flexure coupling length.

(a) Experimental facility

The double flexure coupling-rigid body system is presented in Figure 8a); the flexure couplings (Section 3(a)) can be interchanged with conventional revolute bearing hinges. The first flexure coupling is fixed rigidly and connected to an aluminium profile framework, which is in turn fixed to a bed plate. The rigid bodies comprise of a length of aluminium profile and flexure clamps; the first rigid body also has an actuator attached to the aluminium profile to deflect the second flexure coupling. The first flexure coupling
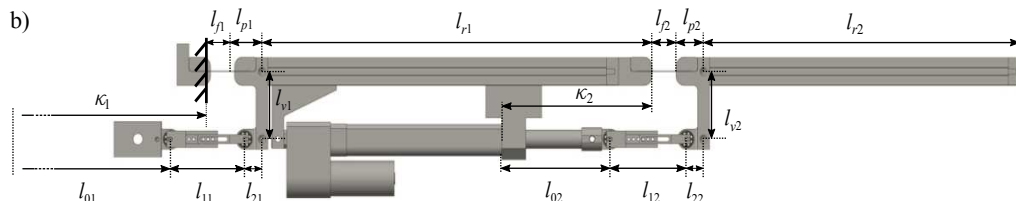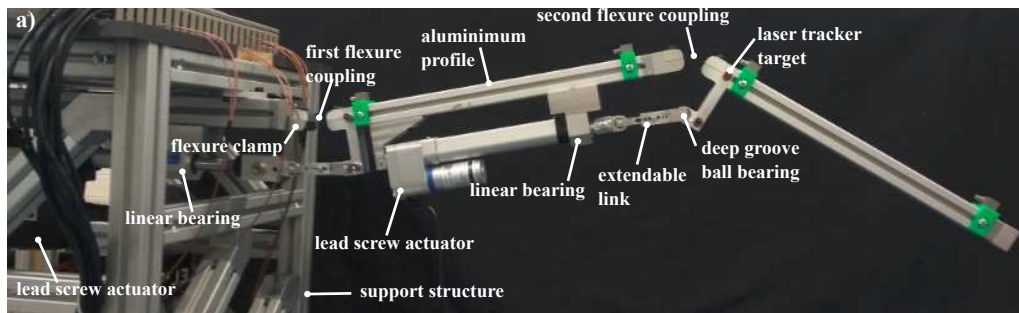
Figure 8. a) Experimental facility for double flexure coupling-rigid body system with components annotated and b) system parameters for mathematical model.

is deflected by an actuator fixed to the framework before the first joint. Both actuators are lead screw devices and have a linear bearing supporting the actuation rod to minimise any side load, and are connected to the rigid body through a linkage mechanism. The extension of the actuator rod over time is controlled using proprietary hardware.

The position of the system is measured using a 3D laser tracker, accurate to within ±0.02 mm; for static tests the laser tracker targets are positioned on the system as shown in Figure 8a), whereas for the dynamic test a single laser tracker target is positioned on the rightmost end of the system and tracked during the complete motion. Figure 8b) shows the system parameters for the mathematical model. The parameter values used in the model, taken from the physical system, are given in Table 1; the flexure coupling properties are stated in Section 3.

Table 1. Parameter values for the standard configuration of the mathematical model.

| Variable	Parameter	Value	Parameter	Value
rigid body length	l_{r1}	500 mm	l_{r2}	450 mm
rigid body mass	m_1	2.585 kg	m_2	0.650 kg
centre of mass along centreline	x_{a1}	204.6 mm	x_{a2}	197.6 mm
centre of mass below centreline	y_{a1}	48.0 mm	y_{a2}	75.0 mm
rigid body moment of inertia	I_{c1}	0.177 kgm^2	I_{c2}	0.0167 kgm^2
offset of actuator rod	κ_1	-184 mm	κ_2	-150 mm
lengths of linkage mechanism	l_{11}	93.0 mm	l_{12}	93.0 mm
members	l_{21}	21.5 mm	l_{22}	21.5 mm
	l_{v1}	73.0 mm	l_{v2}	73.0 mm
	l_{p1}	34.6 mm	l_{p2}	34.6 mm
acceleration due to gravity	g	9.81 m/s^2		
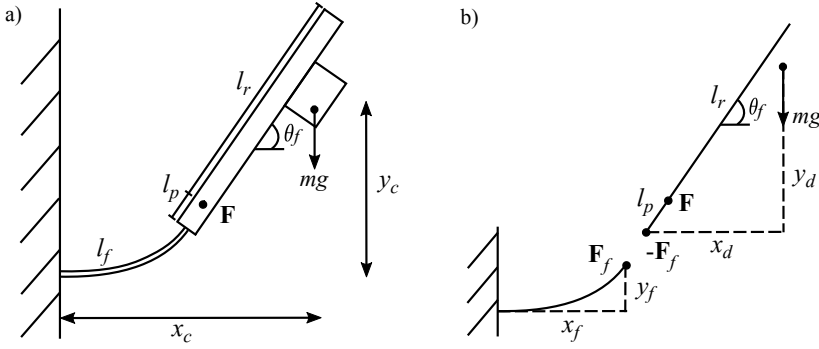
Figure 9. Schematic of a) the centreline of the single flexure coupling-rigid body system geometry and b) corresponding free body diagrams. $\mathbf{F}$ and $\mathbf{F}_f$ are as in Figure 5b).

(b) Single flexure coupling-rigid body system model

Initially, a model for a single rigid body connected with a flexure coupling to a fixed point is formulated; the mass of the flexure is assumed negligible compared to that of the rigid body resulting a pseudo-steady system. The single flexure coupling-rigid body system is shown in Figure 9a), with the corresponding free body diagrams showing the centreline of the system given in Figure 9b). The centre of mass of the rigid body may be offset from the centreline either due to geometric considerations or an actuator attached to a rigid link; a generic case is considered for the derivation of the dynamic governing equations where the centre of mass is positioned at a distance (x_d, y_d) from the end of the rigid body in (x,y) coordinates. The resulting coordinates of the centre of mass are

$$
\begin{aligned}
x_c &= x_f + x_d = x_f + x_a \cos\theta_f + y_a \sin\theta_f, \\
y_c &= y_f + y_d = y_f + x_a \sin\theta_f - y_a \cos\theta_f,
\end{aligned}
\tag{4.1}
$$

where x_a and y_a are the distances of the centre of mass along and perpendicular to the rigid body, respectively.

The time dependent force $\mathbf{F}(t) = (F_N(t), F_M(t), M_C(t))^T$ is found using equations in (3.6) for an imposed force $F_A(t)$ from the actuator through the actuation mechanism given in Figure 5b). The corresponding moment M at an arc length of s at a given time is specified by equation (3.2). The flexure characteristics do not have explicit time dependence, however, the set of internal forces $\mathbf{F}_f = (F_{fx}, F_{fy}, F_{f\theta})^T$ imposed on the end of the flexure from the rigid body may change with time due to the dynamics of the rigid body, giving the flexure coupling implicit time dependence. The equations of motion of the rigid body, when considered as a free body are

$$
\begin{aligned}
m\ddot{x}_c &= -F_{fx} + F_N, \\
m\ddot{y}_c &= -F_{fy} + F_M - mg, \\
I_c\ddot{\theta}_f &= M_C - F_{f\theta} + (F_N - F_{fx})(y_d - l_p\sin\theta_f) - (F_M - F_{fy})(x_d - l_p\cos\theta_f),
\end{aligned}
\tag{4.2}
$$

where I_c is the moment of inertia about the centre of mass.

Equations (4.2) lead to expressions for the internal forces, which can be substituted into (3.2)-(3.3) to give the corresponding governing equations for the pseudo-rigid system and boundary conditions,

$$
\begin{aligned}
EI\theta''(s,t) &= (F_N - m\ddot{x}_f)\sin\theta - (F_M - mg - m\ddot{y}_f)\cos\theta \\
&\quad + m(x_a(\ddot{\theta}_f\cos(\theta_f - \theta) - \dot{\theta}_f^2\sin(\theta_f - \theta)) + y_a(\ddot{\theta}_f\sin(\theta_f - \theta) + \dot{\theta}_f^2\cos(\theta_f - \theta))), \\
EI\theta'(l_f,t) &= M_C - I_c\ddot{\theta}_f - F_N l_p\sin\theta_f + F_M l_p\cos\theta_f - m(x_a^2 + y_a^2)\ddot{\theta}_f \\
&\quad + m(\ddot{x}_f(x_a\sin\theta_f - y_a\cos\theta_f) - (\ddot{y}_f + g)(x_a\cos\theta_f + y_a\sin\theta_f)),
\end{aligned}
$$

$$\theta(0,t) = 0, \tag{4.3}$$

where $'$ denotes differentiation with respect to s. The time derivatives of the centre of mass coordinates are

$$\ddot{x}_c = \ddot{x}_f - \ddot{\theta}_f y_d - \dot{\theta}_f^2 x_d,$$
$$\ddot{y}_c = \ddot{y}_f + \ddot{\theta}_f x_d - \dot{\theta}_f^2 y_d. \tag{4.4}$$

The dynamic behaviour of the flexure system is identified by solving equations (4.3) together with the Cartesian coordinates equations of the flexure (3.1) and corresponding boundary conditions. Discretising this set of equations in the temporal variable and solving over the spatial variable via a boundary value problem solver at every time step over the required time span will give a complete dynamic solution.

New variables are introduced as the position and angle at the end of the flexure coupling are unknown; $z_1 = \theta$, $z_2 = d\theta/ds$, $\eta(s,t) = z_{f1}(t) - z_1(s,t)$, $X(s,t) = x_f(t) - x(s,t)$ and $Y(s,t) = y_f(t) - y(s,t)$, where subscript f denotes the end of the flexure ($s = l_f$). This gives solutions without constraints on the flexure coupling behaviour. Time derivatives are discretised using a backward finite difference approximation with error of $O(\triangle t^2)$ giving the first and second time derivatives of the form,

$$\dot{z}_{f1}(t) = \frac{-3(\eta(s,t) + z_1(s,t))/2 + 2z_{f1}(t - \triangle t) - z_{f1}(t - 2\triangle t)/2}{\triangle t^2} + O(\triangle t^2),$$

$$\ddot{z}_{f1}(t) = \frac{2(\eta(s,t) + z_1(s,t)) - 5z_{f1}(t - \triangle t) + 4z_{f1}(t - 2\triangle t) - z_{f1}(t - 3\triangle t)}{\triangle t^2} + O(\triangle t^2), \tag{4.5}$$

where $\triangle t$ is the time step. Similar expressions are derived for $\ddot{x}_f$ and $\ddot{y}_f$.

The resulting set of first order differential equations to be solved is

$$\frac{dz_1}{ds} = z_2, \qquad \frac{dx}{ds} = \cos z_1, \qquad \frac{dy}{ds} = \sin z_1, \qquad \frac{d\eta}{ds} = -z_2, \qquad \frac{dX}{ds} = -\cos z_1, \qquad \frac{dY}{ds} = -\sin z_1,$$

$$\frac{dz_2}{ds} = \frac{1}{EI}\Big((F_N - m\ddot{x}_f)\sin z_1 - (F_M - mg - m\ddot{y}_f)\cos z_1 + mx_a(\ddot{z}_{f1}\cos(z_{f1} - z_1) - \dot{z}_{f1}^2\sin(z_{f1} - z_1))$$

$$+ my_a(\ddot{z}_{f1}\sin(z_{f1} - z_1) + \dot{z}_{f1}^2\cos(z_{f1} - z_1))\Big),$$

$$\frac{dl_0}{ds} = 0, \qquad \frac{d\phi}{ds} = 0. \tag{4.6}$$

Corresponding boundary conditions

$$z_1(0,t) = 0, \qquad x(0,t) = 0, \qquad y(0,t) = 0, \qquad \eta(l_f,t) = 0, \qquad X(l_f,t) = 0, \qquad Y(l_f,t) = 0,$$

$$z_2(l_f,t) = \frac{1}{EI}(M_C - I_c\ddot{z}_{f1} - F_N l_p\sin z_{f1} + F_M l_p\cos z_{f1} - m(x_a^2 + y_a^2)\ddot{z}_{f1}$$

$$+ m(\ddot{x}_f(x_a\sin z_{f1} - y_a\cos z_{f1}) - (\ddot{y}_f + g)(x_a\cos z_{f1} + y_a\sin z_{f1})),$$

$$l_0(l_f,t) + l_1\cos\phi(l_f,t) = x_f - \kappa + (l_p - l_2)\cos z_{f1} + l_v\sin z_{f1},$$

$$l_1\sin\phi(l_f,t) = y_f + (l_p - l_2)\sin z_{f1} + l_v - l_v\cos z_{f1}, \tag{4.7}$$

with time derivatives of the form in (4.5). For a given initial estimate and set of initial conditions, the set of equations and corresponding boundary conditions (4.6)-(4.7) are solved using a finite difference method implementing a three-stage Lobatto IIIa formula over the arc length at each given time step in the time span.

(c) Double flexure coupling-rigid body system model

Similar methodology can be applied for the double flexure coupling-rigid body system to formulate a dynamic mathematical model; a schematic of the system is given in Figure 10. For deflecting the first flexure coupling, the relationship between the actuator force F_{A1} and force $\mathbf{F}_{f1}$ is given by the equations in (3.6) with the angle ϕ_1 and actuator displacement l_{01} given by (3.8), but with additional subscript 1. A similar actuation mechanism is used to deflect the second joint but is rotated through angle θ_{f1}, giving the
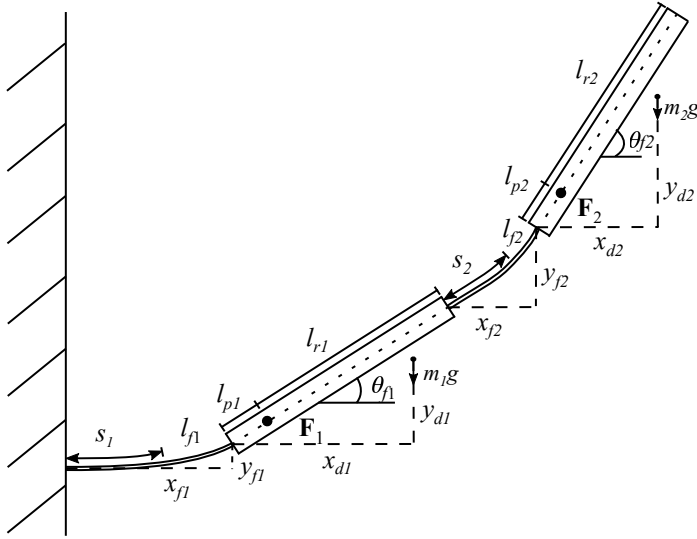
Figure 10. Schematic of the double flexure coupling-rigid body system.

force at the end of second actuation linkage as $\mathbf{F}_{f2} = (F_{N2}, F_{M2}, M_{C2})^T$ in terms of the actuator force F_{A2},

$$F_{N2} = \frac{F_{A2} \cos \phi_2}{\cos(\theta_{f1} - \phi_2)}, \quad F_{M2} = \frac{F_{A2} \sin \phi_2}{\cos(\theta_{f1} - \phi_2)}, \quad M_{C2} = \frac{F_{A2}(l_{22} \sin(\theta_{f2} - \phi_2) + l_{v2} \cos(\theta_{f2} - \phi_2))}{\cos(\theta_{f1} - \phi_2)}, \quad (4.8)$$

with the angle ϕ_2 and the extension of actuator rod l_{02} computed using

$$l_{p2}(\cos \theta_{f1} + \cos \theta_{f2}) + x_{f2} = l_{02} \cos \theta_{f1} + l_{v2} \sin \theta_{f1} + l_{22} \cos \theta_{f2} + l_{12} \cos \phi_2 - l_{v2} \sin \theta_{f2},$$

$$l_{p2}(\sin \theta_{f1} + \sin \theta_{f2}) + y_{f2} = l_{02} \sin \theta_{f1} - l_{v2} \cos \theta_{f1} + l_{22} \sin \theta_{f2} + l_{12} \sin \phi_2 + l_{v2} \cos \theta_{f2}. \quad (4.9)$$

where subscript 2 denotes the second flexure coupling and second rigid body.

Again new variables are defined to account for the end positions of the flexures not being known: $z_{1,3} = \theta_{1,2}$, $z_{2,4} = \theta_{1,2}'$, $\eta_{1,2}(s_{1,2}, t) = z_{f1,f3}(t) - z_{1,3}(s_{1,2}, t)$, $X_{1,2}(s_{1,2}, t) = x_{f1,f2}(t) - x_{1,2}(s_{1,2}, t)$ and $Y_{1,2}(s_{1,2}, t) = y_{f1,f2}(t) - y_{1,2}(s_{1,2}, t)$. Following similar methodology to that for a single flexure coupling-rigid body system the resulting governing equations of the system are a set of first order ordinary differential equations as given in the Appendix.

A comparison between the theoretical predictions and experimental results of the static position of the double flexure coupling-rigid body system for different actuator displacements is given in Figure 11. The experimental results were achieved by displacing the actuators by a given amount and using the laser tracker to measure the position of the system to within ± 0.02 mm. The corresponding model predictions were computed using a look up table for each actuator giving the relationship between the input actuator force F_{A1}, F_{A2}, actuator rod extension l_{01}, l_{02} and the result end position and angle of the flexures $(x_{f1}, y_{f1}, \theta_{f1}), (x_{f2}, y_{f2}, \theta_{f2})$. Using these look up tables allows the overall predicted position of the flexure to be defined. Figure 11 shows good correlation between the theoretical predictions and experimental results with the greatest discrepancy between the two when the first actuator has a large positive displacement.

5. Trajectory control

Attention is now given to the problem of controlling the motion of the double flexure coupling-rigid body system introduced in Section 4. It is desired to control the system such that the end of the system follows a demand trajectory. To demonstrate the feasibility of using flexure couplings the problem is also examined in a corresponding system with conventional revolute bearing hinges. The following double jointed-rigid body systems (DR) are considered:
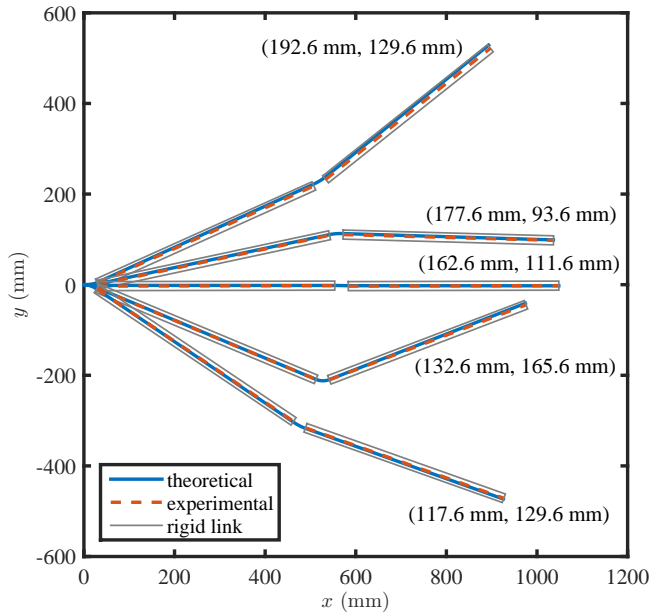
Figure 11. Comparison between the theoretical predictions and experimental results of the static positions of the double flexure coupling-rigid body system for actuator rod extension (l_{01} mm, l_{02} mm).

(i)   incorporating flexure couplings as in Section 4 (DR_F);
(ii) incorporating loosely fitted plain bushing hinges, which exhibit backlash of approximately 0.1 mm on a nominal 8 mm diameter (DR_L);
(iii) incorporating hinges whose rolling elements bearings have been pressed tightly into their housing resulting in zero backlash, but possible torque ripple effects arising from race distortions (DR_P).

In practice conventional bearing hinges will exhibit the characteristics of those in the DR_L and DR_P in varying degrees due to tolerance variability, wear or manufacturing/assembly errors.

Both the DR_L and DR_P may be represented using methodology similar to that in Section 4 with idealised hinge assumptions; the prevailing imperfections of these hinges is generally unknown, and the characteristics change over time with wear so a more realistic model of the hinges is not used. Feedforward control inputs, namely the actuator rod extensions, can then be calculated for the end of the system to follow prescribed trajectories.

For a system incorporating large deflection flexure couplings, it is not sufficient to use a motion controller designed for a comparable system based on conventional bearing joints. That is, a DR_F system cannot be adequately controlled by a controller designed to be used for a DR_L and DR_P systems. Instead, a dedicated motion controller which explicitly takes into account the complex behaviour of the flexible couplings is required. This is demonstrated by Figure 12 where two demand trajectories for the end of the system to follow are specified by:

(a) a circular trajectory with radius of 25 mm over $t_d = 5$ s given by $x_p = 25\cos(2\pi t/t_d - \pi/2)$ mm, $y_p = 25\sin(2\pi t/t_d - \pi/2)$ mm;
(b) a linear trajectory with length 400 mm over $t_d = 13$ s given by $x_p = 1000$ mm, $y_p = 200\sin(2\pi t/t_d - \pi/2)$ mm.

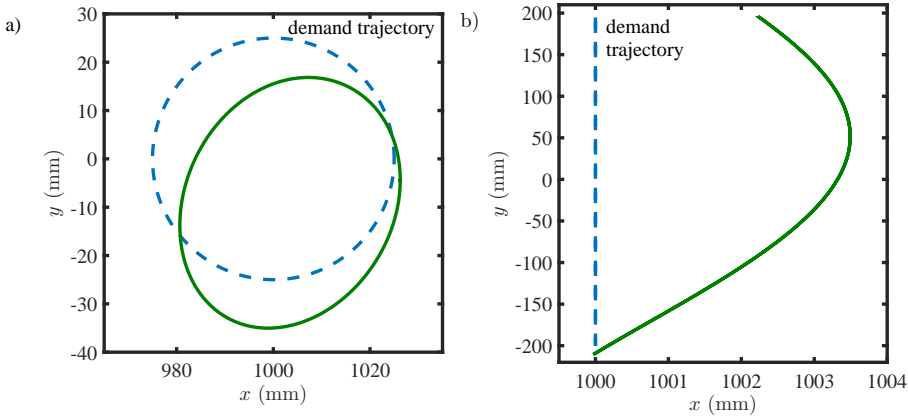The feedforward control inputs required to cause a conventional idealised hinge system to follow these

Figure 12. Predicted position of the end of a DR$_F$ under feedforward control derived using an idealised hinge model: a) circular trajectory and b) linear trajectory, showing that a dedicated model based controller is required for accurate tracking.

demand trajectories have been calculated and applied to a DR$_F$ system model. The simulated responses are shown in Figure 12, with significant displacement errors arising in the predicted trajectory of a DR$_F$ system.

To achieve a better performance, the controller strategy must be based on a model incorporating flexure couplings; thus accounts for their complex behaviour. As such, the model derived in Section 4 is used to compute the required extensions of the actuator rods l_{01} and l_{02} needed for the end of the system to follow a prescribed trajectory $(x_p(t), y_p(t))$. In turn this leads to the end of the second flexure having the trajectory $(x_p(t) - (l_{p2} + l_{r2}) \cos \theta_{f2}(t), y_p(t) - (l_{p2} + l_{r2}) \sin \theta_{f2}(t))$. An additional set of equations needs to be solved simultaneously with the governing equations (A 1) and (A 2), together with equations (3.6) and (4.8) describing the actuation linkage, which are given by

$$\frac{dF_{A1}}{ds} = 0, \quad \frac{dF_{A2}}{ds} = 0;$$
$$0 = x_{p2} - (y_p - (l_{p2} + l_{r2}) \cos \theta_{f2}), \quad 0 = y_{p2} - (y_p - (l_{p2} + l_{r2}) \sin \theta_{f2}). \tag{5.1}$$

These equations impose the constraint of the end trajectory of the system, and that the forces F_{A1}, F_{A2} are independent of the arc length. Solving via a boundary value problem solver at each time step gives the forces F_{A1}, F_{A2} and actuator displacements l_{01}, l_{02} required to move the end position of the system along the desired path. These values can be used in the feedforward control scheme.

To compute the required extensions of the actuator rods over the time span, i.e. the values of l_{01} and l_{02} over t_d, for the DR$_F$ the set of equations (A 1), (A 2) and (5.1) with equations for the actuation linkages (3.6) and (4.8) are solved. A similar set of equations is solved for the system incorporating idealised hinges.

An experimental programme was undertaken to examine the performance of the three DRs. The straight line demand trajectory (Figure 12b) is investigated and the laser tracker is used to measure the realised motion of the end of the system for all experimental runs. It is noted that the linear actuators driving the system exhibit substantially non-ideal performance, including backlash, drift and vulnerability to signal noise. To have them follow the calculated feedforward control paths as closely as possible, the actuators themselves operate under a proportional feedback loop; onboard potentiometers measure the actual actuator extensions, and this signal is subtracted from the extension commanded by the feedforward control scheme to form an error signal on which the feedback loop operates [29]. The feedback gain value is a balance between being large enough to give the system good dynamic tracking performance, and being small enough to avoid amplifying imperfections in the actuators' characteristics.

Figure 13 shows the three DRs performance when operated under a feedforward controller designed on the idealised hinge system model. The experimental response of the DR$_F$ (Figure 13a) is seen to be similar
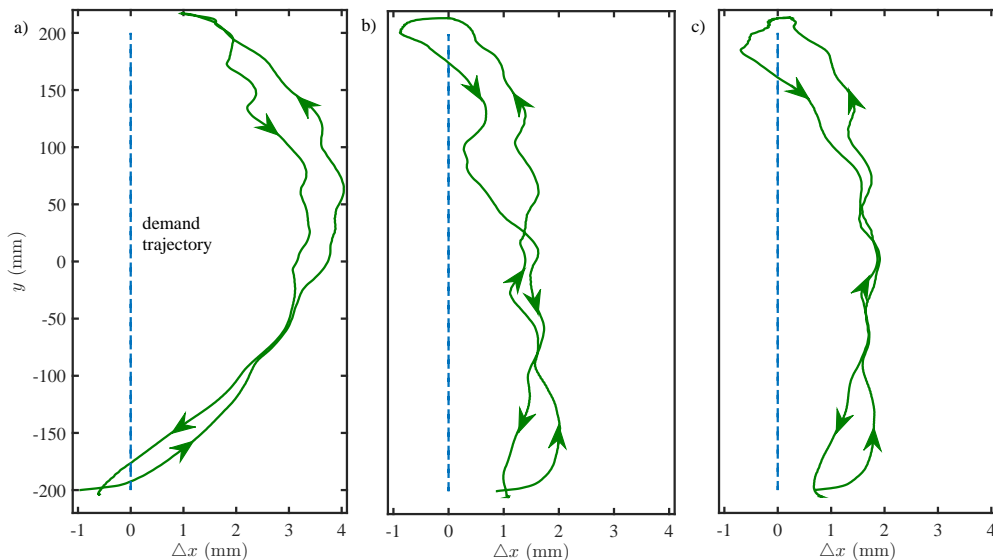
Figure 13. Experimental linear trajectory control error $\triangle x$ for all joint types when feedforward control was derived using an idealised hinge assumption and implemented for a) DR_F, b) DR_L and c) DR_P.
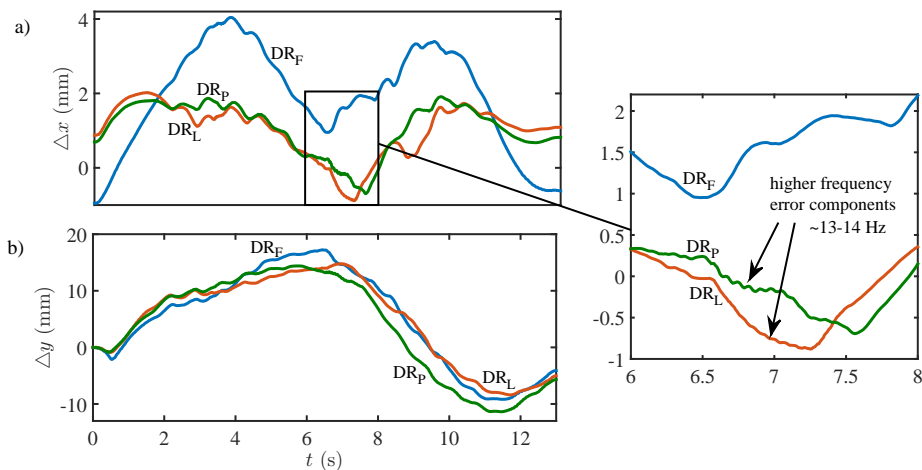

Figure 14. Measured linear trajectory error a) $\triangle x$ and b) $\triangle y$ over time. Feedforward control was derived using an idealised hinge assumption and applied to a DR_F, DR_L and DR_P.

to the theoretical prediction shown in Figure 12b), i.e. a distinct deviation from the demanded trajectory is evident. Results for the DR_L and DR_P show smaller errors for $\triangle x$, which arise due to a combination of actuator uncertainty, non-idealised hinges (L and P) and model errors. The errors are relatively small in the x direction compared to the range of movement in the y direction, but again shows the necessity of a specific feedforward control methodology for a flexure coupling to achieve accurate positioning.

Figure 14 shows the errors in the position of the end of the system compared to the demand trajectory over time for the x and y coordinates. The error in the y direction is significantly larger than that in the
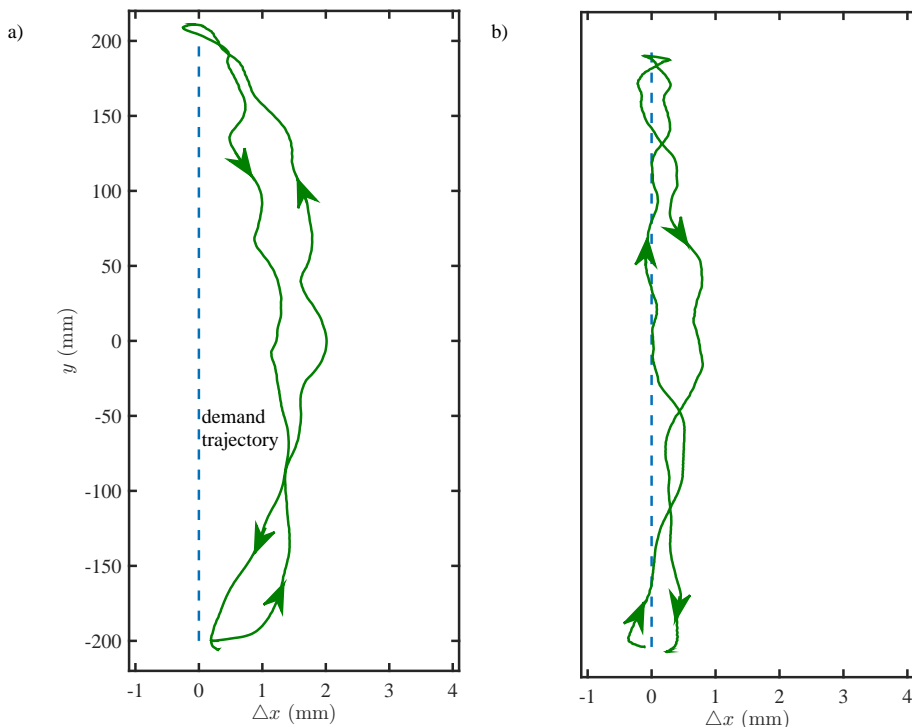
Figure 15. Measured linear trajectory control error $\triangle x$ for a DR_F with a) feedforward control derived using the flexure coupling model and b) implemented with a demand correction to minimise the displacement error.

x direction; all cases have a similar trend for $\triangle y$, but the flexure coupling has different behaviour to the two hinge cases for $\triangle x$. The magnified window view in Figure 14 highlights an example of high frequency behaviour, at $\sim 13 - 14$ Hz, which corresponds to a natural frequency of the system. Excitation sources originate from the nonlinear effects of the hinged components, for example, torque ripple/stick-slip and backlash. When a flexure coupling is used, which does not exhibit these characteristics, far less excitation is evident. In the experimental tests these frequencies were persistent and associated more with a limit cycle response rather than a structural instability. Note that these high frequency components would be amplified in corresponding acceleration profiles (not shown).

Figure 15a) shows the end trajectory for a DR_F when applying the corresponding feedforward control for the actuator rod extensions derived using the flexure coupling model, for a linear trajectory demand with additional proportional feedback; see Supplementary Material for a corresponding video of the system motion. The realised trajectory is closer than that achieved with the idealised hinge control in Figure 13a); the out of plane motion was minimal. The realised trajectory has small errors arising from a combination actuator capabilities/non-smooth actuation and control based on an imperfect model. The errors associated with the feedfoward control action can be reduced further, as in Figure 15b), by subtracting the measured linear trajectory control error $\triangle x$, $\triangle y$ from the desired trajectory; the modified feedforward control is then computed. Results show an improvement in the realised trajectory, which was repeatable over multiple cycles. The remaining error between the demand and realised trajectory is dominated by the actuator capabilities/non-smooth actuation.

6. Conclusions

A novel formulation of a flexure-coupled multibody system is presented, incorporating a model of a flexure coupling undergoing large nonlinear elastic deflections. This was validated experimentally using a bespoke facility having force detection and laser tracking capabilities. Assessments were made of an individual flexure under actuation and an actuated dynamic double flexure-coupled rigid link system. The validation process demonstrated that the nonlinear models had sufficient fidelity to be utilised for control of prescribed rigid link trajectories.

The control methodology comprised of feedforward control, identified from the validated models, and proportional feedback of actuator rod extensions. Although flexure couplings may be alternatives for idealised hinges, feedforward control based on idealised hinge assumptions gives rise to errors in the achieved rigid link trajectories. If the same control is applied to traditional rotary joints, smaller errors are incurred. However, high frequency behaviour was evident in the measurements, corresponding to a natural frequency of the system. Excitation sources originate from the nonlinear effects of the hinged components, for example, torque ripple/stick-slip and backlash. The flexure coupling system did not experience such high frequency effects. The design of feedforward control of a flexure-coupled system incorporating a flexure coupling model is therefore important and a reduction of tracking error was noted when applied. Further reduction of the measured tracking error with flexure couplings was also achieved using a modified input tracking profile and shown to be repeatable over multiple cycles.

The study has therefore demonstrated that flexure couplings have the potential to replace traditional revolute joints in robotic and other automated systems, if they are able to sustain dynamic loading envelopes. Furthermore, they do not experience the same tribological effects such as torque ripple, backlash or wear of traditional joints, hence offer maintenance-free functionality.

Ethics. No ethical considerations apply.

Data Accessibility. Experimental data can be provided as electronic Supplementary Material.

Competing Interests. The authors' declare that there are no competing interests.

Authors' Contributions. All authors designed the research programme. N.Y.B developed the numerical simulations; C.L. and N.Y.B. performed the experimental test under guidance of P.S.K.. All authors contributed to the preparation of the manuscript and approval for submission.

Acknowledgements. No additional acknowledgements.

A. Appendix

The governing equations of the double flexure coupling-rigid body system model are the following set of first order ordinary differential equations

$$
\begin{array}{llll}
z_1' = z_2, & z_2' = \dfrac{F_{1T}}{E_1 I_1}, & x_1' = \cos z_1, & y_1' = \sin z_1, \\[2mm]
\eta_1' = -z_2, & X_1' = -\cos z_1, & Y_1' = -\sin z_1, & \\[2mm]
z_3' = z_4, & z_4' = \dfrac{F_{2T}}{E_2 I_2}, & x_2' = \cos(z_3), & y_2' = \sin(z_3), \\[2mm]
\eta_2' = -z_4, & X_2' = -\cos(z_3), & Y_2' = -\sin(z_3). & \\[2mm]
l_{01}' = 0, & \phi_1{}' = 0, & l_{02}{}' = 0, & \phi_2{}' = 0,
\end{array} \tag{A 1}
$$

with corresponding boundary conditions

$$
z_1(0,t) = 0, \qquad z_2(l_{f1},t) = \frac{\bar{F}_{\theta 1}}{E_1 I_1}, \qquad x_1(0,t) = 0 \qquad y_1(0,t) = 0,
$$

$$
\eta_1(l_{f1},t) = 0, \qquad X_1(l_{f1},t) = 0, \qquad Y_1(l_{f1},t) = 0,
$$

$$
z_3(0,t) = \theta_{f1}, \qquad z_4(l_{f2},t) = \frac{\bar{F}_{\theta 2}}{E_2 I_2}, \qquad x_2(0,t) = x_{f1} + (l_{p1}+l_{r1})\cos\theta_{f1}, \qquad y_2(0,t) = y_{f1} + (l_{p1}+l_{r1})\sin\theta_{f1},
$$

$$\eta_2(l_{f2},t) = \theta_{f1}, \ X_2(l_{f2},t) = x_{f1} + (l_{p1}+l_{r1})\cos\theta_{f1}, \quad Y_2(l_{f2},t) = y_{f1} + (l_{p1}+l_{r1})\sin\theta_{f1},$$

$$l_{01}(l_{f1},t) + l_{11}\cos\phi_1(l_{f1},t) = x_{f1} - \kappa + (l_{p1}-l_{21})\cos z_{f1} + l_{v1}\sin z_{f1},$$

$$l_{11}\sin\phi(l_{f1},t) = y_{f1} + (l_{p1}-l_{21})\sin z_{f1} + l_{v1} - l_{v1}\cos z_{f1},$$

$$l_{02}(l_{f2},t)\cos z_{f1} + l_{12}\cos\phi_2(l_{f2},t) = l_{p2}(\cos z_{f1}+\cos z_{f2}) + x_{f2} - l_{v2}\sin z_{f1} - l_{22}\cos z_{f2} + l_{v2}\sin z_{f2},$$

$$l_{02}(l_{f2},t)\sin z_{f1} + l_{12}\sin\phi_2(l_{f2},t) = l_{p2}(\sin z_{f1}+\sin z_{f2}) + y_{f2} + l_{v2}\cos z_{f1} - l_{22}\sin z_{f2} - l_{v2}\cos z_{f2}. \tag{A 2}$$

In (A 1) and (A 2) the functions F_{1T}, F_{2T}, $F_{\theta 1}$ and $F_{\theta 2}$ are given by

$$
\begin{aligned}
F_{1T} =\ & (F_{N1}+F_{N2})\sin z_1 - (F_{M1}+F_{M2})\cos z_1 - (m_1\ddot{x}_{f1}+m_2(2\ddot{x}_{f1}+\ddot{x}_{f2}))\sin z_1 \\
& + (m_1(\ddot{y}_{f1}+g)+m_2(2\ddot{y}_{f1}+\ddot{y}_{f2}+g))\cos z_1 + m_2(l_{p1}+l_{r1})(\ddot{\theta}_{f1}\cos\eta_1 - \dot{\theta}_{f1}^2\sin\eta_1) \\
& + m_1\ddot{\theta}_{f1}(x_{a1}\cos\eta_1 + y_{a1}\sin\eta_1) - m_1\dot{\theta}_{f1}^2(x_{a1}\sin\eta_1 - y_{a1}\cos\eta_1) \\
& + m_2\ddot{\theta}_{f2}(x_{a2}\cos(\eta_2+z_3-z_1) + y_{a2}\sin(\eta_2+z_3-z_1)) \\
& - m_2\dot{\theta}_{f2}^2(x_{a2}\sin(\eta_2+z_3-z_1) - y_{a2}\cos(\eta_2+z_3-z_1)),
\end{aligned}
$$

$$
\begin{aligned}
F_{2T} =\ & F_{N2}\sin z_3 - F_{M2}\cos z_3 - m_2(\ddot{x}_{f1}+\ddot{x}_{f2})\sin z_3 + m_2(\ddot{y}_{f1}+\ddot{y}_{f2}+g)\cos z_3 - m_2\dot{\theta}_{f2}^2(x_{a2}\sin\eta_2 - y_{a2}\cos\eta_2) \\
& + m_2(l_{p1}+l_{r1})(\ddot{\theta}_{f1}\cos(\eta_1+z_1-z_3) + \dot{\theta}_{f1}^2\sin(\eta_1+z_1-z_3)) + m_2\ddot{\theta}_{f2}(x_{a2}\cos\eta_2 + y_{a2}\sin\eta_2),
\end{aligned}
$$

$$
\begin{aligned}
F_{\theta 1} =\ & M_{C1} + M_{C2} - I_{c1}\ddot{\theta}_{f1} - I_{c2}\ddot{\theta}_{f2} + m_1\ddot{x}_{f1}(x_{a1}\sin(\eta_1+z_1) - y_{a1}\cos(\eta_1+z_1)) \\
& - m_1(g+\ddot{y}_{f1})(x_{a1}\cos(\eta_1+z_1) + y_{a1}\sin(\eta_1+z_1)) \\
& + F_{M2}(X_2+x_2 + (l_{p1}+l_{r1})\cos(\eta_1+z_1) + l_{p2}\cos(\eta_2+z_3)) + F_{M1}l_{p1}\cos(\eta_1+z_1) \\
& - F_{N2}(Y_2+y_2 + (l_{p1}+l_{r1})\sin(\eta_1+z_1) + l_{p2}\sin(\eta_2+z_3)) - m_1\ddot{\theta}_{f1}(x_{a2}{}^2+y_{a2}{}^2) - F_{N1}l_{p1}\sin(\eta_1+z_1) \\
& - (m_2 g + m_2(\ddot{y}_{f1}+\ddot{y}_{f2}))(X_2+x_2 + (l_{p1}+l_{r1})\cos(\eta_1+z_1) + x_{a2}\cos(\eta_2+z_3) + y_{a2}\sin(\eta_2+z_3)) \\
& + m_2(\ddot{x}_{f1}+\ddot{x}_{f2}))(Y_2+y_2 + (l_{p1}+l_{r1})\sin(\eta_1+z_1) + x_{a2}\sin(\eta_2+z_3) - y_{a2}\cos(\eta_2+z_3)) \\
& - m_2(\ddot{y}_{d2} + (l_{p1}+l_{r1})(\ddot{\theta}_{f1}\cos\theta_{f1} - \dot{\theta}_{f1}^2\sin(\eta_1+z_1)))(X_2+x_2) \\
& - m_2(\ddot{x}_{d2} + (l_{p1}+l_{r1})(\ddot{\theta}_{f1}\sin(\eta_1+z_1) + \dot{\theta}_{f1}^2\cos(\eta_1+z_1)))(Y_2+y_2) \\
& - m_2(l_{p1}+l_{r1})(\ddot{\theta}_{f1}+\ddot{\theta}_{f2})(x_{a2}\cos(\eta_2+z_3-\eta_1-z_1) + y_{a2}\sin(\eta_2+z_3-\eta_1-z_1)) - m_2\ddot{\theta}_{f1}(l_{p1}+l_{r1})^2 \\
& - m_2(l_{p1}+l_{r1})(\dot{\theta}_{f1}^2-\dot{\theta}_{f2}^2)(x_{a2}\sin(\eta_2+z_3-\eta_1-z_1) - y_{a2}\cos(\eta_2+z_3-\eta_1-z_1)) - m_2\ddot{\theta}_{f2}(x_{a2}{}^2+y_{a2}{}^2),
\end{aligned}
$$

$$
\begin{aligned}
F_{\theta 2} =\ & M_{C2} - I_{c2}\ddot{\theta}_{f2} - m_2\ddot{\theta}_{f2}(x_{a2}{}^2+y_{a2}{}^2) - F_{N2}l_{p2}\sin(\eta_2+z_3) + F_{M2}l_{p2}\cos(\eta_2+z_3) \\
& + m_2(\ddot{x}_{f1}+\ddot{x}_{f2})(x_{a2}\sin(\eta_2+z_3) - y_{a2}\cos(\eta_2+z_3)) \\
& - (m_2 g + m_2(\ddot{y}_{f1}+\ddot{y}_{f2}))(x_{a2}\cos(\eta_2+z_3) + y_{a2}\sin(\eta_2+z_3)) \\
& - m_2(l_{p1}+l_{r1})\ddot{\theta}_{f1}(x_{a2}\cos(\eta_2+z_3-\eta_1-z_1) + y_{a2}\sin(\eta_2+z_3-\eta_1-z_1)) \\
& - m_2(l_{p1}+l_{r1})\dot{\theta}_{f1}^2(x_{a2}\sin(\eta_2+z_3-\eta_1-z_1) - y_{a2}\cos(\eta_2+z_3-\eta_1-z_1)). \tag{A 3}
\end{aligned}
$$

Expressions for the time derivatives are found using backward finite difference approximations of second order with time step $\triangle t$, with similar form to those in (4.5).

References

1. Herfst R, Dekker B, Witvoet G, Crowcombe W, de Lange D, Sadeghian H. 2015 A miniaturized, high frequency mechanical scanner for high speed atomic force microscope using suspension on dynamically determined points. *Review of Scientific Instruments* **86**, 113703.
2. Fantner GE, Schitter G, Kindt JH, Ivanov T, Ivanova K, Patel R, Holten-Andersen N, Adams J, Thurner PJ, Rangelow IW, Hansma PK. 2006 Components for high speed atomic force microscopy. *Review of Scientific Instruments* **106**, 881-7.
3. Kim JJ, Choi YM, Ahn D, Hwang B, Gweon DG, Jeong J. 2010 A millimeter-range flexure-based nano-positioning stage using a self-guided displacement amplification mechanism. *Mechanism and Machine Theory* **50**, 109-20.

4. Liarokapis MV, Dollar AM. 2016 Post-Contact, In-hand object motion compensation with adaptive hands. *IEEE Transactions on Automation Science and Engineering* **99**, 1-12.

5. Odhner LU, Jentoft LP, Claffee MR, Corson Ni, Tenzer Y, Ma RR, Buehler M, Kohout R, Howe RD, Dollar AM. 2014 A compliant, underactuated hand for robust manipulation. *The International Journal of Robotics Research* **33**, 736-752.

6. Spiers AJ, Liarokapis MV, Calli B, Dollar AM. 2016 Single-grasp object classification and feature extraction with simple robot hands and tactile sensors. *IEEE Transactions on Haptics* **9**, 207-220.

7. Trease BP, Moon YM, Kota S. 2005 Design of large-displacement compliant joints. *Journal of mechanical design* **127**, 788-798.

8. Howell LL, Midha A. 1994 A method for the design of compliant mechanisms with small-length flexural pivots. *IJournal of mechanical design* **116(1)**, 280-290.

9. Mochiyama H. 2016 Model validation of discretized spatial closed elastica. *Intelligent Robots and Systems (IROS), 2016 IEEE/RSJ International Conference on*, 5216–5223.

10. Guo J, Lee KM. 2013 Compliant joint design and flexure finger dynamic analysis using an equivalent pin model. *Mechanism and Machine Theory* **70**, 338-353.

11. Venkiteswaran VK, Su HJ. 2016 A three-spring pseudorigid-body model for soft joints with significant elongation effects. *Journal of Mechanisms and Robotics* **8**, 061001.

12. Wang J, Chen JK, Liao S. 2008 An explicit solution of the large deformation of a cantilever beam under point load at the free tip. *Journal of Computational and Applied Mathematics* **212**, 320-330.

13. Kimiaeifar A, Domairry G, Mohebpour SR, Sohouli AR, Davodi AG. 2011 Analytical solution for large deflections of a cantilever beam under nonconservative load based on homotopy analysis method. *Numerical Methods for Partial Differential Equations* **27**, 541-553.

14. Argyris JH, Symeonidis Sp. 1981 Nonlinear finite element analysis of elastic systems under nonconservative loading-natural formulation. Part I. Quasistatic problems. *Computer Methods in Applied Mechanics and Engineering* **26**, 75-123.

15. Odhner LU, Dollar AM. 2012 The smooth curvature model: an efficient representation of Euler-Bernoulli flexures as robot joints. *IEEE Transactions on Robotics* **28**, 761-772.

16. Rao BN, Rao GV. 1988 Applicability of static or dynamic criterion for the stability of a non-uniform cantilever column subjected to a tip-concentrated subtangential follower force. *Journal of Sound and Vibration* **122**, 188-191.

17. Rao BN, Shastry BP, Rao GV. 1986 Large deflections of a cantilever beam subjected to a tip concentrated rotational load. *The Aeronautical Journal (1968)* **90**, 262-266.

18. Shvartsman BS. 2007 Large deflections of a cantilever beam subjected to a follower force. *Journal of Sound and Vibration* **304**, 969-973.

19. Shvartsman BS. 2013 Analysis of large deflections of a curved cantilever subjected to a tip-concentrated follower force. *International Journal of Non-Linear Mechanics* **50**, 75-80.

20. Ma F, Chen G. 2016 Modeling large planar deflections of flexible beams in compliant mechanisms using chained beam-constraint-model. *Journal of Mechanisms and Robotics* **8**, 021018.

21. Srpčič S, Saje M. 1986 Large deformations of thin curved plane beam of constant initial curvature. *International Journal of Mechanical Sciences* **28**, 275-287.

22. Lobontiu N. 2001 Distributed-parameter dynamic model and optimized design of a four-link pendulum with flexure hinges. *Mechanism and Machine Theory* **36**, 653-669.

23. Armanini C, Dal Corso F, Misseroni D, Bigoni D. 2017 From the elastica compass to the elastica catapult: an essay on the mechanics of soft robot arm. *In Proc. R. Soc. A* **473**, 20160870.

24. Gravagne IA, Rahn CD, Walker ID. 2003 Post-contact, large deflection dynamics and control for planar continuum robots. *IEEE/ASME Transactions on Mechatronics* **8**, 299-307.

25. Moallem M, Kermani MR, Patel RV, Ostojic M. 2004 Flexure control of a positioning system using piezoelectric transducers. *IEEE Transactions on Control Systems Technology* **12**, 757-762.

26. Moallem M, Lu J. 2005 Application of shape memory alloy actuators for flexure control: theory and experiments. *IEEE/ASME Transactions on Mechatronics* **10**, 495-501.

27. Fertis DG. 2007. Nonlinear structural engineering: with unique theories and methods to solve effectively complex nonlinear problems. *Springer Science & Business Media*.

28. Bisshopp KE, Drucker DC. 1945 Large deflection of cantilever beams. *Quarterly of Applied Mathematics* **3**, 272-275.

29. Åström, KJ, Hägglund T. 1995. PID controllers: theory, design, and tuning (Vol. 2). *Research Triangle Park, NC: Instrument Society of America.*